Research Square

Preprints are preliminary reports that have not undergone peer review.
They should not be considered conclusive, used to inform clinical practice,
or referenced by the media as validated information.

Domain-coordinated control strategy based on adaptive yaw moment distribution for fault- tolerant steer-by-wire in over-actuated electric vehicles

Seunguk Jeon
Kookmin University
Yunchul Ha
Kookmin University
Aldo Sorniotti
Polytechnic University
Seunghoon Woo
boltra@kookmin.ac.kr

Kookmin University

Article

Keywords: Adaptive yaw-moment distribution, Domain-coordinated control, Fault tolerant control, Rear wheel steering, Steer-by-wire, Torque vectoring

Posted Date: May 4th, 2026

DOI: https://doi.org/10.21203/rs.3.rs-9398031/v1

License: This work is licensed under a Creative Commons Attribution 4.0 International License.
Read Full License

Additional Declarations: No competing interests reported.

scientific reports

Domain-coordinated control strategy based on adaptive yaw moment distribution for fault-tolerant steer-by-wire in over-actuated electric vehicles

Seunguk Jeon[1], Yunchul Ha[1], Aldo Sorniotti[2], Seunghoon Woo[3]*
[1] Graduate School of Automobile and Mobility, Kookmin University, Seoul 02707, Republic of Korea
[2] Department of Mechanical and Aerospace Engineering, Polytechnic University, Torino, 10129, Italy
[3] Department of Automotive Engineering, Kookmin University, Seoul 02707, Republic of Korea
* Corresponding author: Seunghoon Woo (boltra@kookmin.ac.kr)

Abstract

For electrically actuated steer-by-wire (SbW) systems, fault-tolerant control (FTC) that can handle complete failure is essential for ensuring vehicle safety. Herein, a domain-coordinated FTC strategy based on adaptive yaw-moment distribution is proposed for over-actuated electric vehicles under complete SbW conditions. Unlike conventional SbW-FTC strategies, the proposed strategy improves tracking performance by incorporating the influence of failed actuator dynamics into the control strategy. An integrated state-space model is developed to capture the coupled dynamics of vehicle lateral motion and fault-induced front-wheel steering. Based on this model, the desired yaw moment is adaptively distributed between torque vectoring and rear-wheel steering using real-time sensitivity information that reflects both yaw-moment effectiveness and unintended front-wheel steering according to the driving condition. Simulation results show that compared with the empirically tuned fixed-ratio strategy, the proposed strategy reduces the trajectory-tracking error and yaw-rate tracking error by 6% and 7%, respectively, during a lane-change maneuver. It satisfies the acceptance criterion for the degradation scenario specified in DIN 70065, a functional safety standard for SbW systems. The FTC system with the proposed strategy achieves an average computation time of 0.206 ms in the rapid control prototyping environment, demonstrating real-time feasibility for implementation in production-vehicle microcontroller units.

Keywords Adaptive yaw-moment distribution, Domain-coordinated control, Fault tolerant control, Rear wheel steering, Steer-by-wire, Torque vectoring

Recent advances in vehicle electrification technology have accelerated the development of in-vehicle hardware components, including electronic systems, sensors, and actuators. Although these developments have expanded the functionality of vehicle systems, they have also increased the complexity of hardware configurations and introduced new constraints in terms of packaging and weight.

Steer-by-wire (SbW) systems have been proposed as an alternative to address these issues; these systems eliminate the mechanical connection between the steering mechanism and the front wheels[1]. SbW systems offer several advantages, including vehicle weight reduction, improved packaging efficiency, and effective isolation of road-induced vibration and noise. As SbW systems offers these structural advantages and exhibit control flexibility, they have attracted considerable attention as a vital steering technology for next-generation vehicle systems, including autonomous and electric vehicles[2]. However, similar to other X-by-wire systems, SbW systems rely heavily on electronic components and communication networks; this makes them susceptible to faults such as actuator degradation or loss of function. To ensure vehicle safety under fault conditions, a fault-tolerant control (FTC) strategy that incorporates functional safety must be established[3].

Various approaches have been investigated to ensure the fault tolerance of SbW systems. For example, redundancy

architectures have been applied to SbW motors and microcontrollers to preserve steering functionality even after component faults[4]. Redundant angle and torque sensors have been similarly employed to improve the reliability of steering signals[5]. In addition, FTC strategies have been proposed to internally compensate for tracking errors arising from actuator efficiency degradation and system disturbances under fault conditions[6]. However, although redundancy-based approaches may be effective against single-point faults, they have limited ability in handling multiple faults; they also increase system complexity and cost.

Among the proposed FTC strategies, rear-wheel steering (RWS)-based FTC is widely employed to compensate for the loss of steering functionality in SbW systems. In particular, compensatory RWS angles are generated under SbW fault conditions to preserve path-tracking performance[7]. Reverse-phase RWS control under these conditions can induce unintended front-wheel steering via tire lateral forces, thereby degrading the tracking performance of the FTC system. FTC methods that generate yaw moment using longitudinal differential braking control (DBC)[8] have also been proposed. In these methods, when a large braking force is applied to the inner wheels to generate a yaw moment that assists the vehicle to rotate in the desired turning direction[9]. These DBC strategies have been applied to emergency steering scenarios, and their effectiveness in improving path-tracking performance has been verified via simulation[10].

Recent FTC strategies have exploited over-actuated (OA) vehicle systems that can simultaneously control multiple actuators[11-15]. Based on independently operated drive, brake and steering actuators, control reallocation methods that distribute driving, braking, and steering commands among healthy actuators have been proposed[16]. Similarly, quadratic programming[17] has been employed for control allocation in OA vehicle systems while considering actuator constraints, and model predictive control techniques[18], which incorporate future vehicle state predictions, have been applied to steering-actuator FTC. FTC strategies utilizing multiple actuators offer enhanced vehicle safety and backup steering capability compared with conventional RWS or DBC-based methods[19]. However, under complete SbW failure, in which the steering motor produces no output, unintended front-wheel steering can be induced by the actions of other actuators in the vehicle system. In particular, unintended steering and vehicle dynamic responses vary depending on the control allocation of other actuators, such as wheel driving, braking-force distribution, and RWS inputs. Therefore, the OA vehicle platform requires a control strategy that can reflect in real time the effects of the yaw moments generated by actuator control allocation and unintended steering on the vehicle states. However, studies on FTC strategies that consider unintended steering under SbW faults are limited. In addition, existing FTC studies are limited in their ability to account for vehicle and actuator states in real time within the constrained hardware environments of production vehicles because of the excessive computational burden imposed by algorithmic complexity. To address these limitations, an adaptive yaw-moment distribution (AYD)-based domain-coordinated control (DCC) strategy for OA electric vehicle systems under complete SbW failure.

The main contributions of this study are summarized as follows:

1. Establishment of a complete SbW failure model that incorporates external steering torque induced by scrub and trail moments, and the development of an integrated vehicle model that couples these torque effects with vehicle states and front-wheel steering dynamics.
2. Development of a sensitivity-based AYD law that accounts for yaw-moment response effectiveness and the dynamic effects of unintended steering across varying driving conditions, from transient to steady-state steering.
3. The proposed strategy is verified to satisfy the circle scenario criterion of DIN 70065, a functional safety standard for SbW systems, while also demonstrating real-time computational efficiency suitable for embedded systems in production vehicles.

The remainder of this paper is organized as follows. Section 2 introduces the vehicle model used in the FTC system. Section 3 presents the overall structure of the proposed FTC system and the controller design. Section 4 covers the simulation results and analysis, and Section 5 concludes the paper.

Problem formulation

A complete SbW failure condition is considered herein, in which the steering-actuator motor generates no torque, rather than partial faults such as output reduction or steering-angle locking. Although redundancy-based safety measures are incorporated into steering systems to satisfy the functional safety requirements of ISO 26262[20], they remain insufficient for addressing multiple faults. Accordingly, SbW-FTC strategies that utilize the high degree of control freedom offered by multiactuator-based OA vehicle systems have been extensively studied. In OA vehicle systems, control allocation regulates vehicle dynamics by adjusting individual wheel torques and RWS angles. However, under complete SbW failure, vehicle sideslip induced by control allocation generates lateral forces on the front tires, thereby producing unintended front-wheel steering. This unintended steering considerably impacts the

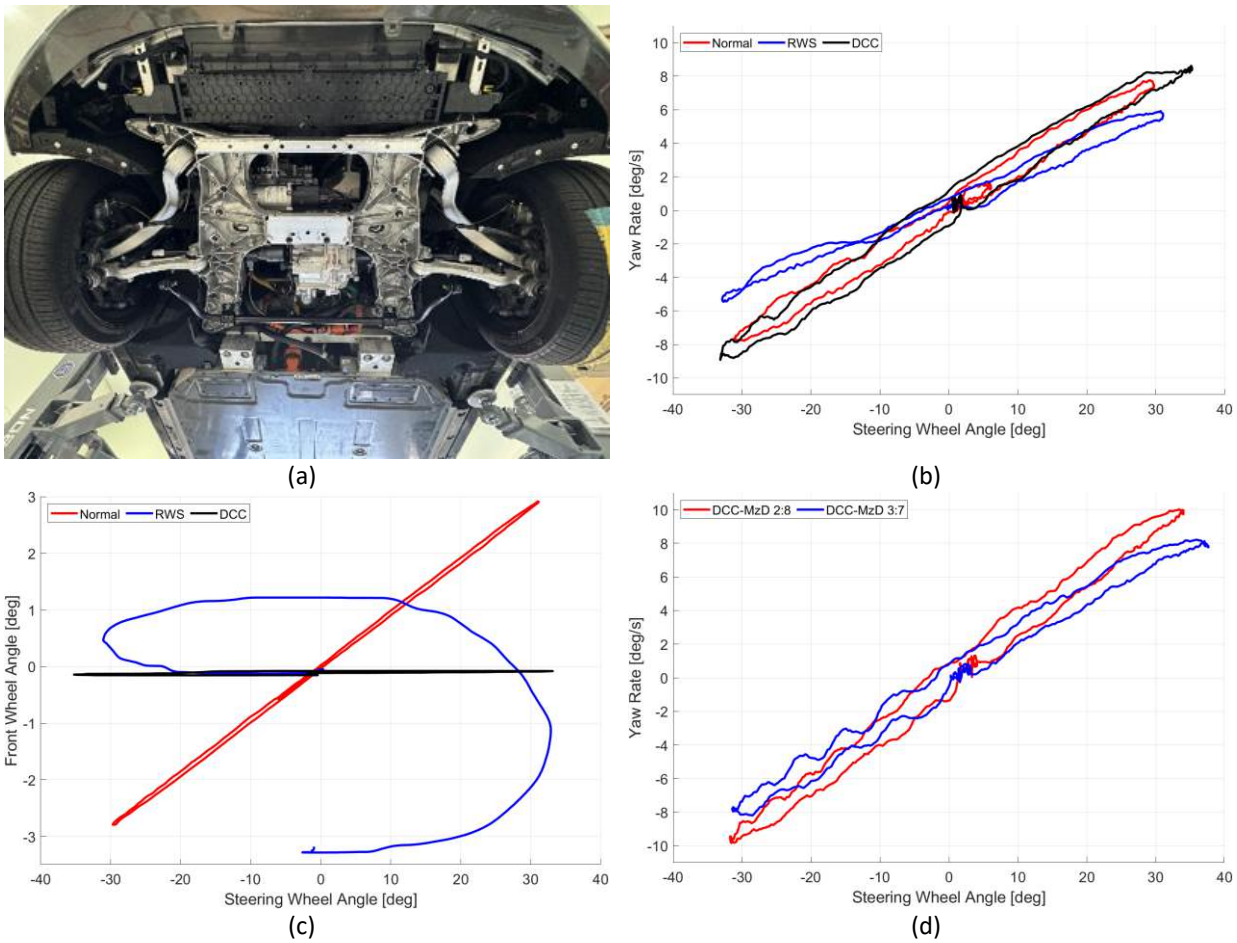


Fig. 1 Experimental results of SbW-FTC in OA electric vehicle system.

vehicle dynamic response. Fig. 1 shows the vehicle motion and front-wheel steering responses under different FTC strategies in an SbW-equipped experimental vehicle. Fig. 1(a) shows the OA electric experimental vehicle. The DCC strategy combines torque vectoring (TV) with RWS, whereas the RWS-based strategy utilizes only the RWS system. Fig. 1(b) shows the yaw-rate responses under normal steering and complete failure conditions with FTC. All FTC strategies exhibit front-wheel steering responses that differ from those under normal steering conditions. Under the RWS strategy, a large front-wheel steering angle is observed in the direction opposite to the intended vehicle turning direction (Fig. 1(c)). Fig. 1(d) shows variations in vehicle dynamic responses as a function of the yaw-moment distribution allocated to each subsystem within the DCC strategy that integrates TV and RWS. These results indicate that vehicle dynamics are sensitive to the actuator control allocation ratio. An FTC system that optimizes control allocation among actuators in real time is developed herein.

Vehicle lateral dynamics

A vehicle lateral dynamics model that represents the SbW system behavior under complete failure conditions is presented herein. Yaw moments generated by left–right differences in driving and braking forces induce vehicle yaw and sideslip dynamics, whereas RWS variations affect the front-wheel steering dynamics.

Fig. 2 shows the four-wheel vehicle model used to represent the lateral motion characteristics of the vehicle system[21]. In this model, v_x and v_y denote the longitudinal and lateral velocities at the vehicle center of gravity (CoG), respectively, β denotes the vehicle sideslip angle, and $\dot{\varphi}$ denotes the yaw rate. δ_f and $\delta_r$denote the front and rear-steering angles, respectively; l_f and l_r denote the distances from the CoG to the front and rear axles, respectively; t_f and t_r are the front and rear track widths, respectively; and m and I_z denote the vehicle mass and yaw moment of inertia, respectively. In addition, $F_{x,i}$ and $F_{y,i}$ $(i = fl, fr, rl, rr)$ denote the longitudinal and lateral tire forces acting on each wheel, respectively. The vehicle model parameters are summarized in Table 1. Based on the Newton–Euler equations and the small-angle assumption, the lateral force and yaw-moment equilibria are expressed as Eqs. (1) and

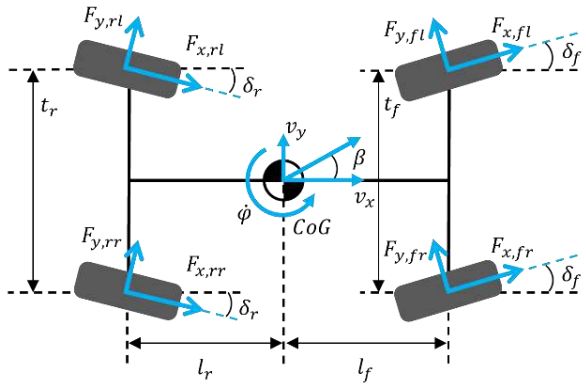


Fig. 2 Vehicle lateral dynamics model representing vehicle motion characteristics.

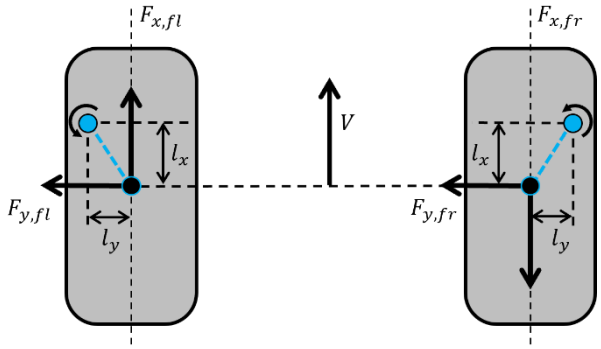


Fig. 3 Simplified front steering system model.

Parameter	Description	Value	Parameter	Description	Value
m	Vehicle mass	2,392 kg	t_f	Front track width	1.630 m
I_z	Yaw moment of inertia	4,740 $kg \cdot m^2$	t_r	Rear track width	1.636 m
l_f	Distance from CG to front axle	1.516 m	C_f	Front tire cornering stiffness	91981 N/rad
l_r	Distance from CG to rear axle	1.474 m	C_r	Rear tire cornering stiffness	79762 N/rad

Table 1. Specifications of the vehicle model.

(2), respectively, and subsequently rearranged into the sideslip rate and yaw-rate dynamics expressed in Eqs. (3) and (4), respectively.

$$mv_x(\dot{\beta} + \dot{\varphi}) = F_{y,f} + F_{y,r} \tag{1}$$

$$I_z\ddot{\varphi} = l_f F_{y,f} - l_r F_{y,r} + \frac{t_f}{2}(F_{x,fr} - F_{x,fl}) + \frac{t_r}{2}(F_{x,rr} - F_{x,rl}) \tag{2}$$

$$\dot{\beta} = -\frac{2(C_f + C_r)}{mv_x}\beta + \left(\frac{2(C_r l_r - C_f l_f)}{mv_x^2} - 1\right)\dot{\varphi} + \frac{2C_f}{mv_x}\delta_f + \frac{2C_r}{mv_x}\delta_r \tag{3}$$

$$\ddot{\varphi} = -\frac{2(C_f l_f - C_r l_r)}{I_z}\beta - \frac{2(C_f l_f^2 + C_r l_r^2)}{I_z v_x}\dot{\varphi} + \frac{2C_f l_f}{I_z}\delta_f - \frac{2C_r l_r}{I_z}\delta_r + \frac{1}{I_z}\left(\frac{t_f}{2}\Delta F_{x,f} + \frac{t_r}{2}\Delta F_{x,r}\right) \tag{4}$$

Fig. 3 shows the front-wheel steering dynamics of the road wheel actuator (RWA) that incorporates the suspension geometry characteristics of the SbW system. The scrub radius l_y denotes the lateral distance between the center of the tire contact patch and the steering axis, and the mechanical trail l_x is the longitudinal distance between the intersection point of the steering axis with the ground and the center of the tire contact patch. As the front wheels rotate about the scrub radius, differences between the left and right braking forces can modify the steering direction[22]. For vehicles with a positive scrub radius, the steering axis intersects the ground inboard of the tire contact patch, whereas for

vehicles with a negative scrub radius, the steering axis intersects outboard. To account for uncertainties in parameters such as friction and cornering stiffness, a simplified steering dynamics model is adopted.

The complete SbW failure condition is modeled by substituting the no-output motor torque condition (Eq. (6)) in the steering dynamics (Eq. (5)). Fault injection is implemented by constraining the RWA motor output to zero, such that no motor torque is generated in response to the driver's steering input. where J_s denotes the steering moment of inertia of the front-wheel steering system, b_s is the steering damping coefficient, and $\dot{\delta_f}$ and $\ddot{\delta_f}$ denote the steering angular velocity and angular acceleration, respectively.

$$J_s\ddot{\delta_f} + b_s\dot{\delta_f} = T_{motor} + T_{ext} \tag{5}$$

$$T_{motor} = 0 \tag{6}$$

The external torque acting on the SbW system under fault conditions is defined in Eq. (7) as the sum of the scrub moment, $T_{scrub,f}$, and the trail moment, T_{trail}. The scrub moment $T_{scrub,f}$ results from the scrub radius and the left–right difference between the front-wheel longitudinal tire forces $\Delta F_{x,f}$. The trail moment T_{trail} denotes the self-aligning moment generated by the total trail acting on the front-wheel lateral tire forces, where $t_{p,f}$ denotes the pneumatic trail of the front tire. The left–right longitudinal force difference at each axle is defined in Eq. (8).

$$T_{ext} = T_{scrub,f} + T_{trail} = l_y\Delta F_{x,f} - \left(l_x + t_{p,f}\right)F_{y,f}^{eq} \tag{7}$$

$$\Delta F_{x,p} = F_{x,pr} - F_{x,pl},\ (p \in \{f, r\}) \tag{8}$$

The equivalent front lateral force $F_{y,f}^{eq}$ in Eq. (9) is not the actual front tire lateral force, but a control-oriented equivalent quantity introduced to represent the unintended steering effect induced by rear-wheel counter-phase steering under SbW fault conditions. Here, C_f and C_r denote the cornering stiffnesses of the front and rear tires, respectively. In Eq. (10), the front tire slip angle α_f is defined as a function of the steering angle, vehicle sideslip angle, yaw rate, and longitudinal velocity.

$$F_{y,f}^{eq} \approx 2C_f\left(\delta_f - \beta - \frac{l_f}{v_x}\dot{\varphi}\right) - 2C_r\delta_r \tag{9}$$

$$\alpha_f = \delta_f - \left(\beta + \frac{l_f}{v_x}\dot{\varphi}\right) \tag{10}$$

By substituting Eqs. (7)–(10) into the steering-axis dynamics, the unintended front-wheel steering motion in the faulted SbW system can be expressed as the second-order differential equation given in Eq. (11). This equation shows that the steering response is directly influenced by the scrub moment arising from the front-wheel longitudinal force difference and by the trail moment associated with the equivalent front lateral force. Rearranging Eq. (11) yields the steering angular acceleration model in Eq. (12), where $\ddot{\delta_f}$ is represented as a linear combination of vehicle state variables, steering-system damping, front differential longitudinal tire forces, and RWS input. This model elucidates the mechanism by which the vehicle longitudinal and lateral dynamics influence the steering behavior under complete SbW failure conditions, thereby providing a theoretical foundation for establishing a DCC FTC strategy.

$$J_s\ddot{\delta_f} + b_s\dot{\delta_f} = l_y\Delta F_{x,f} - \left(l_x + t_{p,f}\right)\left[2C_f\left(\delta_f - \beta - \frac{l_f}{v_x}\dot{\varphi}\right) - 2C_r\delta_r\right] \tag{11}$$

$$\begin{aligned}\ddot{\delta_f} = &-\frac{b_s}{J_s}\dot{\delta_f} - \frac{2C_f\left(l_x + t_{p,f}\right)}{J_s}\delta_f + \frac{2C_f\left(l_x + t_{p,f}\right)}{J_s}\beta + \frac{2C_f l_f\left(l_x + t_{p,f}\right)}{J_s v_x}\dot{\varphi} + \frac{l_y}{J_s}\Delta F_{x,f} \\ &+ \frac{2C_r\left(l_x + t_{p,f}\right)}{J_s}\delta_r\end{aligned} \tag{12}$$

The desired yaw moment is defined as the sum of its longitudinal and lateral components, as expressed in Eq. (13). The longitudinal component, defined in Eq. (14), is generated by the left–right longitudinal force differences at the front and rear axles, weighted by the corresponding half track widths. The lateral component, defined in Eq. (15), is approximated as the yaw moment induced by RWS based on the linear rear tire cornering response.

$$M_{z,des} = M_{z,long} + M_{z,lat} \tag{13}$$

$$M_{z,long} = \frac{t_f}{2}\left(\Delta F_{x,f}\right) + \frac{t_r}{2}\left(\Delta F_{x,r}\right) \tag{14}$$

$$M_{z,lat} \approx -2C_r l_r\delta_r \tag{15}$$

The integrated state-space model of the vehicle lateral dynamics and SbW steering dynamics under fault conditions is given in Eqs. (16)–(18). Under SbW fault conditions, the front-steering angle becomes a state variable rather than a control input and the state vector is defined as $x = \left[\beta, \dot{\varphi}, \dot{\delta}_f, \delta_f\right]^\top$. The state matrix A, defined in Eq. (16), represents the coupled dynamics among vehicle sideslip, yaw, and fault-induced front-wheel steering. The input matrix B, defined in Eq. (17), maps the system control inputs to the integrated state dynamics. The control-input vector is defined as $u = [M_{z,long} \quad M_{z,lat}]^\top$, where the longitudinal and lateral yaw moments are utilized to compensate for the loss of front-wheel steering authority under SbW actuator faults. $k_{lm,f}$ is the front-axle portion of the total longitudinal yaw moment, as expressed in Eq. (18).

$$A = \begin{bmatrix} -\frac{2\left(C_f + C_r\right)}{mv_x} & \frac{2(C_r l_r - C_f l_f)}{mv_x^2} - 1 & 0 & \frac{2C_f}{mv_x} \\ -\frac{2\left(C_f l_f - C_r l_r\right)}{I_z} & -\frac{2\left(C_f l_f^2 + C_r l_r^2\right)}{I_z v_x} & 0 & \frac{2C_f l_f}{I_z} \\ \frac{2C_f\left(l_x + t_{p,f}\right)}{J_s} & \frac{2C_f l_f\left(l_x + t_{p,f}\right)}{J_s v_x} & -\frac{b_s}{J_s} & -\frac{2C_f\left(l_x + t_{p,f}\right)}{J_s} \\ 0 & 0 & 1 & 0 \end{bmatrix} \tag{16}$$

$$B = \begin{bmatrix} 0 & -\frac{1}{mv_x l_r} \\ \frac{1}{I_z} & \frac{1}{I_z} \\ \frac{2k_{lm,f} l_y}{J_s t_f} & -\frac{l_x + t_{p,f}}{J_s l_r} \\ 0 & 0 \end{bmatrix} \tag{17}$$

$$k_{lm,f} = \frac{M_{z,long}^f}{M_{z,long}}, \qquad \left(0 \le k_{lm,f} \le 1\right) \tag{18}$$

FTC system design

FTC architecture

The FTC system developed to handle a complete RWA failure in the SbW system is described herein. The SbW-FTC system is implemented on an OA electric vehicle system with a tri-motor electric all-wheel-drive (e-AWD) configuration, four electromechanical brake (EMB) actuators, and an RWS system. The FTC control architecture comprises four modules: supervisory-, upper-, lower-, and vehicle-level modules, as shown in Fig. 4. The supervisory-level module generates the desired longitudinal and lateral states after fault occurrence, and the upper-level module computes the longitudinal force as well as the longitudinal and lateral yaw moments required to track these states. The lower-level module performs TV-based control allocation, thereby distributing the longitudinal yaw moment into individual wheel torques and converting the lateral yaw moment into an RWS angle.

Reference state definition

The desired vehicle states are defined based on the driver's inputs and the vehicle speed at the time of fault occurrence. $v_{x,des}$ is set to the vehicle speed at the time of fault occurrence, as shown in Eq. (19). The desired lateral behavior is defined by the steady-state yaw rate and sideslip angle, as expressed in Eqs. (20) and (21)[23], where L denotes the vehicle wheelbase.

$$v_{x,des} = v_x\left(t_{fault}\right) \tag{19}$$

$$\dot{\varphi}_{des} = \frac{v_{x,des}}{l_f + l_r + \frac{m{v_x}^2\left(l_r C_r - l_f C_f\right)}{2C_f C_r L}} \delta_{f,des} \tag{20}$$

$$\beta_{des} = \frac{l_r - \frac{l_f m v_{x,des}^2}{2C_r\left(l_f + l_r\right)}}{l_f + l_r + \frac{m{v_x}^2\left(l_r C_r - l_f C_f\right)}{2C_f C_r L}} \delta_{f,des} \tag{21}$$

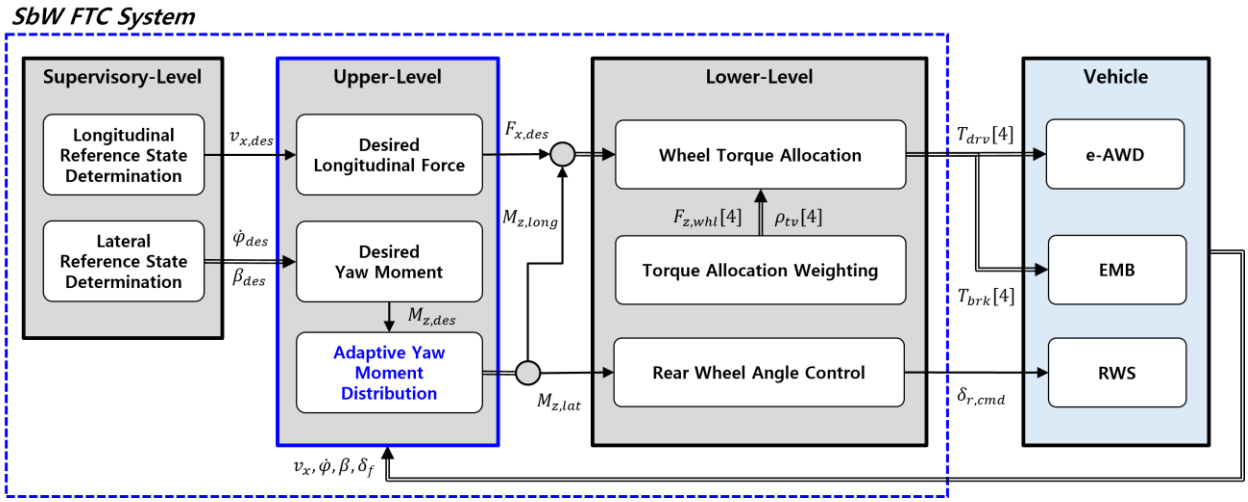


Fig. 4 Architecture of the proposed SbW-FTC system.

Upper-level controller

The upper-level control module generates the desired longitudinal force and yaw moment via a feedback controller designed using a discrete-time linear quadratic regulator[24]. The feedback controller is designed using a state-space model based on the dynamics of yaw rate, sideslip, and longitudinal acceleration.

The lateral dynamics are represented using the discrete-time state-space model expressed in Eq. (22), where the state vector comprises yaw rate and sideslip angle and the control input is the desired yaw moment. The lateral state vector is defined as $x_{lat}(k) = [\dot{\varphi}(k) \quad \beta(k)]^\top$, comprising yaw rate and sideslip angle, and the target state vector is defined as $x_{lat,des}(k) = [\dot{\varphi}_{des}(k) \quad \beta_{des}(k)]^\top$. The lateral state error, $\tilde{x}_{lat}(k) = x_{lat}(k) - x_{lat,des}(k)$, represents the deviation between the current and target vehicle lateral states and is used as the basis for generating the desired yaw moment. The quadratic cost function used to minimize yaw-rate and sideslip-angle tracking errors is defined in Eq. (23).

$$x_{lat}(k+1) = A_{lat}x_{lat}(k) + B_{lat}M_{z,des}(k) \tag{22}$$

$$J_{lat} = \sum_{k=0}^{\infty} \left(\tilde{x}_{lat}^T(k) Q_{lat} \tilde{x}_{lat}(k) + M_{z,des}^T(k) R_{lat} M_{z,des}(k) \right) \tag{23}$$

The optimal solution P is obtained by solving the discrete-time Riccati equation (Eq. (24)), and the corresponding optimal feedback gain K_{lat} is calculated from Eq. (25). Using this gain, the desired yaw moment is generated as the state-feedback control input in Eq. (26). The weighting matrices Q and R are selected to balance tracking performance and control effort.

$$P_{lat} = A_{lat}^\top P_{lat} A_{lat} - A_{lat}^\top P_{lat} B_{lat} \left(R_{lat} + B_{lat}^\top P_{lat} B_{lat} \right)^{-1} B_{lat}^\top P_{lat} A_{lat} + Q_{lat} \tag{24}$$

$$K_{lat} = \left(R_{lat} + B_{lat}^\top P_{lat} B_{lat} \right)^{-1} B_{lat}^\top P_{lat} A_{lat} \tag{25}$$

$$M_{z,des}(k) = -K_{lat} \tilde{x}_{lat}(k) \tag{26}$$

To represent longitudinal dynamics, the longitudinal state vector is defined as $x_{long}(k) = [a_x(k) \quad v_x(k)]^\top$, where a_x nd v_x denote longitudinal acceleration and vehicle speed, respectively. The target state vector is defined as $x_{long,des}(k) = [0 \quad v_{x,des}(k)]^\top$, where the target longitudinal acceleration is set to zero to enable steady-state speed tracking. Accordingly, the longitudinal state error, $\tilde{x}_{long}(k) = x_{long}(k) - x_{long,des}(k)$, is used as the feedback state for computing the desired longitudinal acceleration and, ultimately, the desired longitudinal force. The discrete-time longitudinal state-space model is expressed in Eq. (28).

$$\dot{a}_x(t) = -\frac{1}{\tau} a_x(t) + \frac{1}{\tau} a_{x,des}(t), \quad \left(\dot{v}_x(t) = a_x(t) \right) \tag{27}$$

$$x_{long}(k+1) = A_{long}x_{long}(k) + B_{long}a_{x,des}(k) \tag{28}$$

The formulation of the cost function and the derivation of the optimal solution follow the same process as the yaw-moment generation. To minimize the velocity-tracking error, the quadratic cost function is defined in Eq. (29). The desired longitudinal acceleration is then calculated from the longitudinal state error using Eq. (30), and the desired longitudinal force is finally obtained from the commanded acceleration and vehicle mass, as expressed in Eq. (31).

$$J_{long} = \sum_{k=0}^{\infty} \left(\tilde{x}_{long}^{T}(k) Q_{long} \tilde{x}_{long}(k) + a_{x,des}^{T}(k) R_{long} a_{x,des}(k) \right) \tag{29}$$

$$a_{x,des}(k) = -K_{long} \tilde{x}_{long}(k) \tag{30}$$

$$F_{x,des}(k) = m a_{x,des}(k) \tag{31}$$

Adaptive yaw moment distribution law

The AYD law that accounts for unintended front-wheel steering induced by complete SbW failure using real-time sensitivity weighting is described herein. By decomposing the target yaw-moment computed at the upper level into longitudinal and lateral components, the proposed law generates reference commands required for control allocation in the lower-level subsystems.

The yaw-acceleration and sideslip-rate dynamics, extracted from the state-space model using the selection vectors $e_{\dot{\varphi}}^{\top}$ and $e_{\beta}^{\top}$, are expressed in Eqs. (32) and (33), respectively. Based on these expressions, Eqs. (34) and (35) define the corresponding state-rate sensitivity coefficients with respect to the longitudinal yaw moment $M_{z,long}$, lateral yaw moment $M_{z,lat}$, and front-wheel steering angle δ_f.

$$\ddot{\varphi} = e_{\dot{\varphi}}^{\top} \dot{x} = e_{\dot{\varphi}}^{\top} A x + e_{\dot{\varphi}}^{\top} B_{long} M_{z,long} + e_{\dot{\varphi}}^{\top} B_{lat} M_{z,lat} \tag{32}$$

$$\dot{\beta} = e_{\beta}^{\top} \dot{x} = e_{\beta}^{\top} A x + e_{\beta}^{\top} B_{long} M_{z,long} + e_{\beta}^{\top} B_{lat} M_{z,lat} \tag{33}$$

$$\frac{\partial \ddot{\varphi}}{\partial M_{z,long}} = e_{\dot{\varphi}}^{\top} B_{long} = \frac{1}{I_z}, \qquad \frac{\partial \ddot{\varphi}}{\partial M_{z,lat}} = e_{\dot{\varphi}}^{\top} B_{lat} = \frac{1}{I_z}, \qquad \frac{\partial \ddot{\varphi}}{\partial \delta_f} = e_{\dot{\varphi}}^{\top} A e_{\delta} = \frac{2C_f l_f}{I_z} \tag{34}$$

$$\frac{\partial \dot{\beta}}{\partial M_{z,long}} = e_{\beta}^{\top} B_{long} = 0, \qquad \frac{\partial \dot{\beta}}{\partial M_{z,lat}} = e_{\beta}^{\top} B_{lat} = -\frac{1}{m v_x l_r}, \qquad \frac{\partial \dot{\beta}}{\partial \delta_f} = e_{\beta}^{\top} A e_{\delta} = \frac{2C_f}{m v_x} \tag{35}$$

The static sensitivity of the induced front-wheel steering angle to the distributed yaw-moment inputs is derived using steady-state relationships, as expressed in Eqs. (36)–(38). Under the steady-state assumption, the state derivative is set to zero, and the vehicle lateral dynamics are expressed as the algebraic equilibrium condition in Eq. (36). Rearranging this condition yields Eq. (37), which relates the steady-state vector to the longitudinal and lateral yaw-moment inputs. The steady-state front-wheel steering angle $\delta_{f,ss}$ is extracted from the steady-state vector using the selection vector $e_{\delta}^{\top}$, as defined in Eq. (38).

$$0 = A x_{ss} + B_{long} M_{z,long} + B_{lat} M_{z,lat} \tag{36}$$

$$x_{ss} = -A^{-1} B_{long} M_{z,long} - A^{-1} B_{lat} M_{z,lat} \tag{37}$$

$$\delta_{f,ss} = e_{\delta}^{\top} x_{ss} = e_{\delta}^{\top} \left(-A^{-1} B_{long} M_{z,long} - A^{-1} B_{lat} M_{z,lat} \right) \tag{38}$$

The steady-state sensitivities of the induced front-wheel steering angle to the longitudinal and lateral yaw-moment inputs are defined in Eqs. (39) and (40), respectively. Here, $K_{\delta_{f,ss}}^{long}$ quantifies the effect of $M_{z,long}$ on the steady-state front-wheel steering angle induced by the scrub moment caused by left–right longitudinal force differences, whereas $K_{\delta_{f,ss}}^{lat}$ quantifies the effect of $M_{z,lat}$ on the steady-state front-wheel steering angle induced by the trail moment steering effect.

$$K_{\delta_{f,ss}}^{long} = \frac{\partial \delta_{f,ss}}{\partial M_{z,long}} = e_{\delta}^{\top} (-A^{-1}) B_{long} \approx \left(\frac{k_{lm,f} l_y}{C_f t_f \left(l_x + t_{p,f} \right)} \right) \tag{39}$$

$$K_{\delta_{f,ss}}^{lat} = \frac{\partial \delta_{f,ss}}{\partial M_{z,lat}} = e_{\delta}^{\top} (-A^{-1}) B_{lat} \approx -\frac{1}{2C_f l_r} \tag{40}$$

The transient-state response of the vehicle lateral dynamics model to distributed yaw-moment inputs is expressed in Eqs. (41)–(43). The linear state-transition solution over the prediction horizon T, which accounts for the natural system response and the forced response induced by the yaw-moment input, is expressed in Eq. (41). The zero-order

hold assumption, under which the yaw-moment input is treated as constant over the interval $[0, T]$, is expressed in Eq. (42). Based on this assumption, equation (43) provides an approximate closed-form prediction of the future state; this prediction is subsequently used to derive the dynamic sensitivity of unintended front-wheel steering in the transient phase.

$$x(t+T) = e^{AT}x(t) + \int_0^T e^{A(T-\tau)}\, B_j M_{z,j}(t+\tau) d\tau \tag{41}$$

$$u_j(t+\tau) = M_{z,j}(t+\tau) \approx M_{z,j}(t), \tau \in [0,\, T] \tag{42}$$

$$x(t+T) \approx e^{AT}x(t) + \left(\int_0^T e^{A(T-\tau)}\, d\tau\right) B_j M_{z,j}(t) \tag{43}$$

The dynamic sensitivity of the induced front-wheel steering angle with respect to the distributed yaw-moment inputs is expressed in Eqs. (44)–(48). The finite-time and infinite-time steering sensitivities, which represent the transient and steady-state effects of each distributed yaw-moment input, respectively, are defined in Eq. (44). The corresponding sensitivity matrices over finite and infinite-time horizons, $S(T)$ and $S(\infty)$, are defined as expressed in Eqs. (45) and (46). Using these sensitivities, Eq. (47) defines the transient induced-steering effectiveness coefficient $\tau_{\delta,j}\big(T_r(t)\big)$ as a saturated and normalized measure of the transient steering sensitivity relative to its steady-state counterpart. Equation (48) defines an adaptive response time $T_r(t)$ computed from the ratio of the front-wheel steering angle to its angular velocity. This response time is used to determine whether the current steering response is in a transient or near-steady-state region. A small $T_r(t)$ indicates a rapidly varying transient response, whereas a large $T_r(t)$ indicates convergence toward steady state. The design parameters in Eqs. (47) and (48) are selected as $T_{r,min} = 10^{-2}$, $T_{r,max} = 5$, $\tau_{\delta,min} = -1$, $\tau_{\delta,max} = 1$, and $\epsilon_s = 10^{-6}$.

$$\frac{\partial \delta_f(t+T)}{\partial M_{z,j}(t)} = e_\delta^\top S(T) B_j, \qquad \frac{\partial \delta_f(t+\infty)}{\partial M_{z,j}(t)} = e_\delta^\top S(\infty) B_j \tag{44}$$

$$S(T) = \int_0^T e^{A\tau}\, d\tau = A^{-1}(e^{AT} - I) \tag{45}$$

$$S(\infty) = \int_0^\infty e^{A\tau}\, d\tau = A^{-1}\left(\lim_{T\to\infty} e^{AT} - I\right) = -A^{-1} \tag{46}$$

$$\tau_{\delta,j}\big(T_r(t)\big) = sat\left(\frac{\sigma_{sgn} e_\delta^\top S\big(T_r(t)\big) B_j}{\left|e_\delta^\top (-A^{-1}) B_j\right| + \epsilon_s}, \tau_{\delta,min}, \tau_{\delta,max}\right), \qquad j \in \{long, lat\} \tag{47}$$

$$T_r(t) = sat\left(\frac{\left|\delta_f(t)\right| + \epsilon_s}{\left|\dot{\delta}_f(t)\right| + \epsilon_s}, T_{r,min}, T_{r,max}\right), \qquad \sigma_{sgn} = sgn\big(M_{z,des}\big) \tag{48}$$

The integrated sensitivities, which combine the direct state-rate sensitivity to each yaw-moment component with the indirect contribution arising from induced front-wheel steering, are defined in Eqs. (49)–(53). Equation (49) defines the effective induced-steering sensitivity as the product of the transient effectiveness coefficient $\tau_{\delta,j}$ and the steady-state induced-steering sensitivity $K^j_{\delta_{f,ss}}$. Using this effective term, Eqs. (50)–(53) describe the integrated sensitivities of yaw acceleration and sideslip rate with respect to the longitudinal and lateral yaw-moment components.

$$\left(\frac{\partial \delta_f}{\partial M_{z,j}}\right)_{eff} \coloneqq \tau_{\delta,j} K^j_{\delta_{f,ss}} \tag{49}$$

$$s_{\ddot{\varphi},long} = \left[\frac{\partial \ddot{\varphi}}{\partial M_{z,long}} + \frac{\partial \ddot{\varphi}}{\partial \delta_f}\left(\frac{\partial \delta_f}{\partial M_{z,long}}\right)_{eff}\right] = \frac{1}{I_z} + \tau_{\delta,long}(T_r)\frac{2C_f l_f}{I_z} K^{long}_{\delta_{f,ss}} \tag{50}$$

$$s_{\dot{\beta},long} = \left[\frac{\partial \dot{\beta}}{\partial M_{z,long}} + \frac{\partial \dot{\beta}}{\partial \delta_f}\left(\frac{\partial \delta_f}{\partial M_{z,long}}\right)_{eff}\right] = \tau_{\delta,long}(T_r)\frac{2C_f}{m v_x} K^{long}_{\delta_{f,ss}} \tag{51}$$

$$s_{\ddot{\varphi},lat} = \left[\frac{\partial \ddot{\varphi}}{\partial M_{z,lat}} + \frac{\partial \ddot{\varphi}}{\partial \delta_f}\left(\frac{\partial \delta_f}{\partial M_{z,lat}}\right)_{eff}\right] = \frac{1}{I_z} + \tau_{\delta,lat}(T_r)\frac{2C_f l_f}{I_z} K^{lat}_{\delta_{f,ss}} \tag{52}$$

$$s_{\dot{\beta},lat} = \left[\frac{\partial \dot{\beta}}{\partial M_{z,lat}} + \frac{\partial \dot{\beta}}{\partial \delta_f}\left(\frac{\partial \delta_f}{\partial M_{z,lat}}\right)_{eff}\right] = -\frac{1}{m v_x l_r} + \tau_{\delta,lat}(T_r)\frac{2C_f}{m v_x} K^{lat}_{\delta_{f,ss}} \tag{53}$$

Using the integrated sensitivities defined in Eqs. (49)–(53), the proposed AYD law can predict the state-rate response associated with a given yaw-moment allocation. The corresponding state-rate prediction model is presented in Eqs. (54)–(58). The desired and actual state-rate vectors, composed of yaw acceleration and sideslip rate, are defined in Eq. (54). The desired yaw acceleration and sideslip rate are computed from the difference between the next-step desired states and the current actual states over the sampling interval T_s, as expressed in Eq. (55). Equation (56) presents a first-order local approximation of the state-rate response with respect to a yaw-moment input around the operating point. This formulation is then extended to a distributed-input representation shown in Eq. (57), where the predicted state-derivative vector $\hat{\dot{x}}_s(k|\alpha)$ is obtained by multiplying the integrated sensitivity matrix by the distributed control-input vector. The longitudinal and lateral yaw moments are defined by decomposing the desired total yaw moment $M_{z,des}(k)$ into $M_{z,long}(k)$ and $M_{z,lat}(k)$ using the distribution ratio $\alpha(k)$, as expressed in Eq. (58).

$$\dot{x}_{s,des}(k) = \begin{bmatrix} \ddot{\varphi}_{des}(k) \\ \dot{\beta}_{des}(k) \end{bmatrix}, \qquad \dot{x}_s(k) = \begin{bmatrix} \ddot{\varphi}(k) \\ \dot{\beta}(k) \end{bmatrix} \tag{54}$$

$$\ddot{\varphi}_{des}(k) = \frac{\dot{\varphi}_{des}(k+1) - \dot{\varphi}(k)}{T_s}, \qquad \dot{\beta}_{des}(k) = \frac{\beta_{des}(k+1) - \beta(k)}{T_s} \tag{55}$$

$$\ddot{\varphi}(M_z) \approx \ddot{\varphi}(M_{z,0}) + \left.\frac{\partial \ddot{\varphi}}{\partial M_z}\right|_{M_{z,0}} (M_z - M_{z,0}), \qquad \dot{\beta}(M_z) \approx \dot{\beta}(M_{z,0}) + \left.\frac{\partial \dot{\beta}}{\partial M_z}\right|_{M_{z,0}} (M_z - M_{z,0}) \tag{56}$$

$$\hat{\dot{x}}_s(k|\alpha) = \begin{bmatrix} \hat{\ddot{\varphi}}(k|\alpha) \\ \hat{\dot{\beta}}(k|\alpha) \end{bmatrix} = \begin{bmatrix} s_{\ddot{\varphi},long}(k) & s_{\ddot{\varphi},lat}(k) \\ s_{\dot{\beta},long}(k) & s_{\dot{\beta},lat}(k) \end{bmatrix} M(k,\alpha) \tag{57}$$

$$M(k,\alpha) = \begin{bmatrix} M_{z,long}(k) \\ M_{z,lat}(k) \end{bmatrix} = \begin{bmatrix} \alpha M_{z,des}(k) \\ (1-\alpha) M_{z,des}(k) \end{bmatrix} \tag{58}$$

By substituting the distributed yaw-moment components from Eq. (58) into the state-derivative prediction model in Eq. (57), the predicted yaw acceleration $\hat{\ddot{\varphi}}(k|\alpha)$ and sideslip rate $\hat{\dot{\beta}}(k|\alpha)$ are obtained (Eqs. (59) and (60), respectively). These equations represent the predicted state-rate responses as linear combinations of the longitudinal and lateral integrated sensitivities. Equation (61) defines the corresponding sensitivity differences, $\Delta s_{\ddot{\varphi}}(k)$ and $\Delta s_{\dot{\beta}}(k)$, which quantify the relative change in effectiveness between the longitudinal and lateral yaw-moment components.

$$\hat{\ddot{\varphi}}(k|\alpha) = s_{\ddot{\varphi},long}(k)\alpha M_{z,des}(k) + s_{\ddot{\varphi},lat}(k)(1-\alpha)M_{z,des}(k) = \left(s_{\ddot{\varphi},lat}(k) + \alpha \Delta s_{\ddot{\varphi}}(k)\right) M_{z,des}(k) \tag{59}$$

$$\hat{\dot{\beta}}(k|\alpha) = s_{\dot{\beta},long}(k)\alpha M_{z,des}(k) + s_{\dot{\beta},lat}(k)(1-\alpha)M_{z,des}(k) = \left(s_{\dot{\beta},lat}(k) + \alpha \Delta s_{\dot{\beta}}(k)\right) M_{z,des}(k) \tag{60}$$

$$\Delta s_{\ddot{\varphi}}(k) = s_{\ddot{\varphi},long}(k) - s_{\ddot{\varphi},lat}(k), \qquad \Delta s_{\dot{\beta}}(k) = s_{\dot{\beta},long}(k) - s_{\dot{\beta},lat}(k) \tag{61}$$

The normalized state-rate error used in the proposed AYD law is defined in Eqs. (62)–(66). The normalized error vector $e_x(k,\alpha)$ is obtained by applying the weighting matrix $W_x(k)$ to the deviation between the desired and predicted state derivatives, as expressed in Eq. (62). Here, $W_x(k)$ functions as a normalization factor that scales yaw acceleration and sideslip rate errors into a dimensionless space. The normalization factors $\sigma_{\ddot{\varphi}}(k)$ and $\sigma_{\dot{\beta}}(k)$ are defined as state-rate normalization scales based on the desired yaw-moment magnitude and peak absolute integrated sensitivity for each state variable, as expressed in Eqs. (63) and (64). By combining the desired yaw-moment magnitude with the peak absolute integrated sensitivity to the longitudinal and lateral yaw-moment components, these factors provide normalization scales for the yaw acceleration and sideslip rate. The normalized yaw-acceleration and sideslip rate errors, $e_{\ddot{\varphi}}(k,\alpha)$ and $e_{\dot{\beta}}(k,\alpha)$, are represented in Eqs. (65) and (66), where each error is expressed as an affine function of the yaw-moment distribution ratio $\alpha(k)$.

$$e_x(k,\alpha) = W_x(k)\left(\dot{x}_{s,des}(k) - \hat{\dot{x}}_s(k|\alpha)\right), \qquad W_x(k) = diag\left(\frac{1}{\sigma_{\ddot{\varphi}}(k)+\epsilon_s}, \frac{1}{\sigma_{\dot{\beta}}(k)+\epsilon_s}\right) \tag{62}$$

$$\sigma_{\ddot{\varphi}}(k) = \left|M_{z,des}(k)\right| max\left(\left|s_{\ddot{\varphi},long}(k)\right|, \left|s_{\ddot{\varphi},lat}(k)\right|\right) \tag{63}$$

$$\sigma_{\dot{\beta}}(k) = \left|M_{z,des}(k)\right| max\left(\left|s_{\dot{\beta},long}(k)\right|, \left|s_{\dot{\beta},lat}(k)\right|\right) \tag{64}$$

$$e_{\ddot{\varphi}}(k,\alpha) = \frac{\ddot{\varphi}_{req}(k) - \hat{\ddot{\varphi}}(k|\alpha)}{\sigma_{\ddot{\varphi}}(k)+\epsilon_s} = \frac{\ddot{\varphi}_{req}(k) - M_{z,des}(k)s_{\ddot{\varphi},lat}(k) - \alpha M_{z,des}(k)\Delta s_{\ddot{\varphi}}(k)}{\sigma_{\ddot{\varphi}}(k)+\epsilon_s} \tag{65}$$

$$e_{\dot{\beta}}(k,\alpha) = \frac{\dot{\beta}_{req}(k) - \hat{\dot{\beta}}(k|\alpha)}{\sigma_{\dot{\beta}}(k) + \epsilon_s} = \frac{\dot{\beta}_{req}(k) - M_{z,des}(k)s_{\dot{\beta},lat}(k) - \alpha M_{z,des}(k)\Delta s_{\dot{\beta}}(k)}{\sigma_{\dot{\beta}}(k) + \epsilon_s} \tag{66}$$

For closed-form optimization, the normalized state-rate error expressions are rearranged into a linear form in $\alpha(k)$, as shown in Eq. (67). The coefficients $A_{\ddot{\varphi}}(k)$ and $A_{\dot{\beta}}(k)$ characterize the sensitivity of each normalized state-rate error to $\alpha(k)$, whereas $B_{\ddot{\varphi}}(k)$ and $B_{\dot{\beta}}(k)$ represent the corresponding baseline residual errors when $\alpha(k) = 0$, as expressed in Eqs. (68) and (69).

$$e_{\ddot{\varphi}}(k,\alpha) = B_{\ddot{\varphi}}(k) - A_{\ddot{\varphi}}(k)\alpha, \qquad e_{\dot{\beta}}(k,\alpha) = B_{\dot{\beta}}(k) - A_{\dot{\beta}}(k)\alpha \tag{67}$$

$$A_{\ddot{\varphi}}(k) = \frac{M_{z,des}(k)\Delta s_{\ddot{\varphi}}(k)}{\sigma_{\ddot{\varphi}}(k) + \epsilon_s}, \qquad B_{\ddot{\varphi}}(k) = \frac{\ddot{\varphi}_{des}(k) - M_{z,des}(k)s_{\ddot{\varphi},lat}(k)}{\sigma_{\ddot{\varphi}}(k) + \epsilon_s} \tag{68}$$

$$A_{\dot{\beta}}(k) = \frac{M_{z,des}(k)\Delta s_{\dot{\beta}}(k)}{\sigma_{\dot{\beta}}(k) + \epsilon_s}, \qquad B_{\dot{\beta}}(k) = \frac{\dot{\beta}_{des}(k) - M_{z,des}(k)s_{\dot{\beta},lat}(k)}{\sigma_{\dot{\beta}}(k) + \epsilon_s} \tag{69}$$

The proposed AYD law determines the optimal solution using the weighted least-squares[25] method, and the corresponding optimization criterion is defined in Eqs. (70)–(72). The weighting-based distribution ratio $\alpha_w(k)$ is computed from the relative magnitudes of the longitudinal and lateral sensitivity indices, where each index $\eta_j(k)$ represents the overall effectiveness of the corresponding yaw-moment generation mechanism, as expressed in Eq. (71). The normalized yaw-acceleration and sideslip-rate sensitivity components, $\bar{s}_{\ddot{\varphi},j}(k)$ and $\bar{s}_{\dot{\beta},j}(k)$, are defined by normalizing the integrated sensitivities with the magnitudes of their corresponding steady-state sensitivities for each yaw-moment generation mechanism, as expressed in Eq. (72). Here, $s^{ss}_{\ddot{\varphi},j}$ and $s^{ss}_{\dot{\beta},j}$ denote the steady-state integrated sensitivities of the yaw-acceleration and sideslip-rate responses for each yaw-moment generation mechanism, obtained by evaluating Eqs. (50)–(53) under the steady-state induced-steering condition, i.e., $\tau_{\delta,j} = 1$. This normalization ensures a consistent evaluation of sensitivity indices $\eta_j(k)$ despite differences in units and magnitudes between the state-rate variables.

$$J(\alpha) = w_{\ddot{\varphi}}e_{\ddot{\varphi}}(k,\alpha)^2 + w_{\dot{\beta}}e_{\dot{\beta}}(k,\alpha)^2 + \lambda_{rate}\left(\alpha - \alpha_{prev}\right)^2 + \lambda_w(\alpha - \alpha_w)^2 \tag{70}$$

$$\alpha_w(k) = sat\left(\frac{\eta_{long}(k)}{\eta_{long}(k) + \eta_{lat}(k)}, 0, 1\right), \qquad \eta_j(k) = \sqrt{\bar{s}^2_{\ddot{\varphi},j}(k) + \bar{s}^2_{\dot{\beta},j}(k)} \tag{71}$$

$$\bar{s}_{\ddot{\varphi},j}(k) = \frac{s_{\ddot{\varphi},j}(k)}{\left|s^{ss}_{\ddot{\varphi},j}\right| + \epsilon_s}, \qquad \bar{s}_{\dot{\beta},j}(k) = \frac{s_{\dot{\beta},j}(k)}{\left|s^{ss}_{\dot{\beta},j}\right| + \epsilon_s} \tag{72}$$

The optimal solution to the proposed yaw-moment distribution problem is given in Eqs. (73)–(75). The first-order optimality condition, obtained by differentiating the quadratic objective function with respect to $\alpha(k)$, is expressed in Eq. (73). Solving this condition yields the closed-form distribution ratio in Eq. (74), where the solution is analytically determined from the normalized state-rate error coefficients and the regularization terms associated with the previous allocation ratio and the sensitivity-based reference ratio. Using this optimal ratio, Eq. (75) decomposes the desired total yaw moment into longitudinal and lateral yaw-moment commands for the lower-level subsystems. This approach enables the real-time computation of the yaw-moment allocation ratio without requiring iterative numerical optimization. The objective-function weights in Eqs. (73) and (74) are set to $w_{\ddot{\varphi}} = 0.5$, $w_{\dot{\beta}} = 0.2$, $\lambda_{rate} = 0.1$, and $\lambda_w = 0.2$.

$$\frac{dJ}{d\alpha} = 2w_{\ddot{\varphi}}A_{\ddot{\varphi}}\left(A_{\ddot{\varphi}}\alpha - B_{\ddot{\varphi}}\right) + 2w_{\dot{\beta}}A_{\dot{\beta}}\left(A_{\dot{\beta}}\alpha - B_{\dot{\beta}}\right) + 2\lambda_{rate}\left(\alpha - \alpha_{prev}\right) + 2\lambda_w(\alpha - \alpha_w) = 0 \tag{73}$$

$$\alpha(k) = \frac{w_{\ddot{\varphi}}A_{\ddot{\varphi}}B_{\ddot{\varphi}} + w_{\dot{\beta}}A_{\dot{\beta}}B_{\dot{\beta}} + \lambda_{rate}\alpha_{prev} + \lambda_w\alpha_w}{w_{\ddot{\varphi}}A^2_{\ddot{\varphi}} + w_{\dot{\beta}}A^2_{\dot{\beta}} + \lambda_{rate} + \lambda_w}, \qquad a_{opt}(k) = sat(\alpha(k), 0, 1) \tag{74}$$

$$M_{z,long}(k) = a_{opt}(k)M_{z,des}(k), \qquad M_{z,lat}(k) = \left(1 - a_{opt}(k)\right)M_{z,des}(k) \tag{75}$$

Lower-level controller

The lower-level control module employs quadratic programming[26] to allocate the longitudinal and lateral yaw moments computed by the upper-level controller to the control inputs of the TV and RWS systems, respectively.

The quadratic programming problem used for lower-level longitudinal yaw-moment control allocation is defined in Eqs. (76)–(78). The control allocation objective is expressed as a weighted least-squares problem that minimizes the tracking error between the achieved control output Au and the desired command vector b while penalizing the control effort, as expressed in Eq. (76). In this formulation, the effectiveness matrix A maps the control-input vector u shown in Eq. (77) to the generalized longitudinal control outputs, and the target vector b represents the desired longitudinal force and yaw moment requested by the upper-level controller. The weighting matrices Q and R prioritize tracking performance and penalize control effort, respectively, as defined in Eq. (78).

$$\min_u J = (Au - b)^\top Q(Au - b) + u^\top Ru, \qquad A = \begin{bmatrix} A_{fx} \\ A_{mz} \end{bmatrix}, \qquad b = \begin{bmatrix} F_{x,des} \\ M_{z,long} \end{bmatrix} \tag{76}$$

$$u = [T_{f,drv} \quad T_{fl,brk} \quad T_{fr,brk} \quad T_{rl} \quad T_{rr}]^\top \tag{77}$$

$$Q = diag(q_{fx}, q_{mz}) \in R^{2\times 2}, \qquad R = diag\left(\rho_0, \frac{1}{\rho_{tv,1}}, \frac{1}{\rho_{tv,2}}, \frac{1}{\rho_{tv,3}}, \frac{1}{\rho_{tv,4}}\right) \tag{78}$$

The mapping vectors A_{fx} and A_{mz} convert actuator torque inputs into total longitudinal force and longitudinal yaw moment, respectively, as defined in Eq. (79). The geometric moment arms of each wheel are defined using the vehicle track widths, axle distances, and steering angles, as expressed in Eqs. (80) and (81). The allowable driving and braking torque limits are defined by combining actuator torque bounds with tire friction limits, as expressed in Eqs. (82) and (83). The friction limits are estimated based on the tire vertical load[27] from vehicle accelerometer signals.

$$A_{fx} = \frac{1}{r_{eff}}[cos\,\delta_f \quad cos\,\delta_f \quad cos\,\delta_f \quad cos\,\delta_r \quad cos\,\delta_r], \qquad A_{mz} = \frac{1}{r_{eff}}[0 \quad M_{fl} \quad M_{fr} \quad M_{rl} \quad M_{rr}] \tag{79}$$

$$M_{fl} = -\frac{t_f}{2}cos\,\delta_f + l_f\,sin\,\delta_f, \qquad M_{fr} = \frac{t_f}{2}cos\,\delta_f + l_f\,sin\,\delta_f \tag{80}$$

$$M_{rl} = -\frac{t_r}{2}cos\,\delta_r + l_r\,sin\,\delta_r, \qquad M_{rr} = \frac{t_r}{2}cos\,\delta_r + l_r\,sin\,\delta_r \tag{81}$$

$$T^{lim}_{f,drv} = min\left(T^{max}_{f,drv}, T^{lim}_{w,fl} + T^{lim}_{w,fr}\right), \qquad T^{lim}_{ir,drv} = \min\left(T^{max}_{ir,drv}, T^{lim}_{w,ir}\right), \qquad ir \in \{rl, rr\} \tag{82}$$

$$T^{lim}_{i,brk} = min\left(T^{max}_{i,brk}, T^{lim}_{w,i}\right), \qquad T^{lim}_{w,i} = r_{eff}F^{max}_{x,i}, \qquad i \in \{fl, fr, rl, rr\} \tag{83}$$

The lower and upper bounds u_{min} and u_{max} of the optimization input vector are specified to ensure that each actuator operates within its allowable driving or braking torque range, as expressed in Eqs (84) and (85). The first optimization variable denotes the total front-axle driving torque, which is configured to be equally distributed between the left and right front wheels. Eq. (86) yields the optimal control-input vector $u_{opt,}$ obtained by solving the quadratic programming problem. As the rear-wheel torques are optimized in signed form, they are decomposed into separate driving and braking commands by extracting their positive and negative components in Eqs. (87) and (88), respectively.

$$u_{min} = \left[0 \quad -T^{lim}_{brk,fl} \quad -T^{lim}_{brk,fr} \quad -T^{lim}_{brk,rl} \quad -T^{lim}_{brk,rr}\right]^\top \tag{84}$$

$$u_{max} = \left[T^{lim}_{f,drv} \quad 0 \quad 0 \quad T^{lim}_{rl,drv} \quad T^{lim}_{rr,drv}\right]^\top \tag{85}$$

$$u_{opt} = [T^*_{f,drv} \quad T^*_{fl,brk} \quad T^*_{fr,brk} \quad T^*_{rl} \quad T^*_{rr}]^\top \tag{86}$$

$$T^{cmd}_{d,rl} = max(T^*_{rl}, 0), \qquad T^{cmd}_{d,rr} = max(T^*_{rr}, 0) \tag{87}$$

$$T^{cmd}_{b,rl} = max(-T^*_{rl}, 0), \qquad T^{cmd}_{b,rr} = max(-T^*_{rr}, 0) \tag{88}$$

The simplified sensitivity-based weighting model for TV control allocation is defined in Eqs. (89)–(92). Eq. (89) expresses an approximate steady-state relationship between the state vector and the four-wheel longitudinal tire-force vector using the reduced gain matrix G_{ss}. Here, the TV input u_{tv} is defined as the vector of individual longitudinal tire forces, $u_{tv} = [F_{x,fl} \quad F_{x,fr} \quad F_{x,rl} \quad F_{x,rr}]^{\mathrm{T}}$. For weighting computation, B_{tv} is intentionally constructed as an approximate input matrix. Specifically, it retains only the dominant direct yaw-moment contribution of the four longitudinal tire forces and the direct scrub-induced steering-axis moment caused by front-wheel longitudinal force differences, while neglecting higher-order and indirect lateral-state coupling effects. Accordingly, the second row of B_{tv} is given by $\left[-\frac{t_f}{2I_z} \quad \frac{t_f}{2I_z} \quad -\frac{t_r}{2I_z} \quad \frac{t_r}{2I_z}\right]$ and the third row is $\left[-\frac{l_y}{J_s} \quad \frac{l_y}{J_s} \quad 0 \quad 0\right]$. From this reduced model, Eq. (90) extracts the yaw-rate sensitivity row $G_{ss,\dot{\varphi}}$, whose elements $K_{\dot{\varphi},i}$ are used as approximate weighting indices that indicate the relative contribution of each wheel's longitudinal force to the steady-state yaw-rate response. Based on these indices, the normalized front and rear-wheel weights $\rho_{tv,}$ on the left and right sides of the vehicle are defined in Eqs. (91) and (92), respectively.

$$x_{ss} = -A^{-1}B_{tv}u_{tv}, \qquad G_{ss} = -A^{-1}B_{tv} \tag{89}$$

$$\dot{\varphi}_{ss} = e_{\dot{\varphi}}^{\top}x_{ss} = \left[e_{\dot{\varphi}}^{\top}(-A^{-1}B_{tv})\right]u_{tv}, \qquad G_{ss,\dot{\varphi}} = [K_{\dot{\varphi},fl} \quad K_{\dot{\varphi},fr} \quad K_{\dot{\varphi},rl} \quad K_{\dot{\varphi},rr}] \tag{90}$$

$$\rho_{tv,1} = \frac{\left|K_{\dot{\varphi},fl}\right|}{\left|K_{\dot{\varphi},fl}\right| + \left|K_{\dot{\varphi},rl}\right|}, \quad \rho_{tv,2} = \frac{\left|K_{\dot{\varphi},fr}\right|}{\left|K_{\dot{\varphi},fr}\right| + \left|K_{\dot{\varphi},rr}\right|} \tag{91}$$

$$\rho_{tv,3} = \frac{\left|K_{\dot{\varphi},rl}\right|}{\left|K_{\dot{\varphi},fl}\right| + \left|K_{\dot{\varphi},rl}\right|}, \quad \rho_{tv,4} = \frac{\left|K_{\dot{\varphi},rr}\right|}{\left|K_{\dot{\varphi},fr}\right| + \left|K_{\dot{\varphi},rr}\right|} \tag{92}$$

The RWS allocation for lateral yaw-moment generation and front-steering compensation is defined in Eqs. (93)–(95). Using simplified linear-tire approximation, the yaw-moment effectiveness of RWS is defined by considering only the rear-steering contribution to the rear lateral tire force and the corresponding lateral yaw moment, as expressed in Eq. (93). The RWS angle is decomposed into two primary components: $\delta_{r,m}(k)$ for generating the assigned lateral yaw moment and $\delta_{r,c}(k)$ for offsetting the unintended front-wheel steering (Eq. (94)). Here, $\delta_{f,un}(k)$ denotes the unintended front-wheel steering angle under SbW-FTC conditions. A weighting factor for the compensatory steering term is introduced based on the lateral yaw-moment allocation ratio, as expressed in Eq. (95). The design parameters are $\rho_{min} = 0.3$, $\rho_{max} = 0.8$, $w_{\delta,min} = 0$, and $w_{\delta,max} = 0.5$. Here, ρ_{min} and ρ_{max} define the activation range of the lateral yaw-moment allocation ratio, whereas $w_{\delta,min}$ and $w_{\delta,max}$ denote the lower and upper bounds of the compensatory RWS weight, respectively.

$$F_{y,r}(k) \approx 2C_r\delta_r(k), \qquad M_{z,lat}(k) \approx -l_rF_{y,r}(k) = -2C_rl_r\delta_r(k) \tag{93}$$

$$\delta_{r,m}(k) = \frac{M_{z,lat}(k)}{G_r}, \qquad \delta_{r,c}(k) = -\frac{G_f}{G_r}\delta_{f,un}(k), \qquad G_f = 2C_fl_f, \qquad G_r = -2C_rl_r \tag{94}$$

$$\rho_\delta(k) = 1 - a_{opt}(k), \qquad w_\delta(k) = w_{\delta,min} + (w_{\delta,max} - w_{\delta,min})sat\left(\frac{\rho_\delta(k) - \rho_{min}}{\rho_{max} - \rho_{min}}, 0{,}1\right) \tag{95}$$

The RWS component $\delta_{r,m}(k)$ for lateral yaw-moment generation is constrained within the allowable rear-steering range to obtain the saturated command $\delta_{r,m}^{p}(k)$, as expressed in Eq. (96). The available steering margin for additional compensation is computed using Eq. (97). The compensatory RWS component $\delta_{r,c}^{p}(k)$ is constrained to not exceed the available steering margin and is combined with the yaw-moment-generating component to obtain the final RWS command $\delta_{r,cmd}(k)$, as expressed in Eq. (98).

$$\delta_{r,m}^{p}(k) = sat\left(\delta_{r,m}(k), \delta_{r,min}, \delta_{r,max}\right), \tag{96}$$

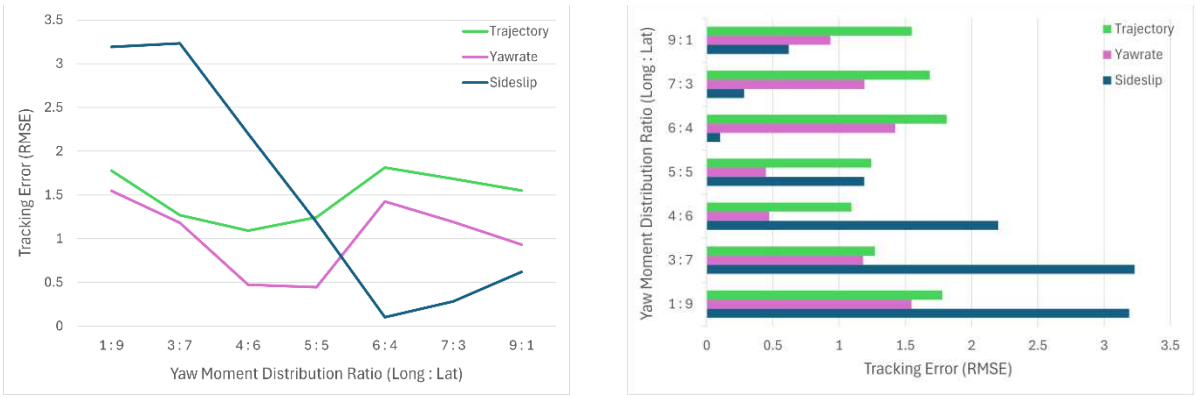
$$\Delta\delta_r^{-}(k) = \delta_{r,min} - \delta_{r,m}^{p}(k), \qquad \Delta\delta_r^{+}(k) = \delta_{r,max} - \delta_{r,m}^{p}(k), \tag{97}$$

$$\delta_{r,c}^{p}(k) = sat\left(w_\delta(k)\delta_{r,c}(k), \Delta\delta_r^{-}(k), \Delta\delta_r^{+}(k)\right), \delta_{r,cmd}(k) = \delta_{r,m}^{p}(k) + \delta_{r,c}^{p}(k) \tag{98}$$

Simulation results

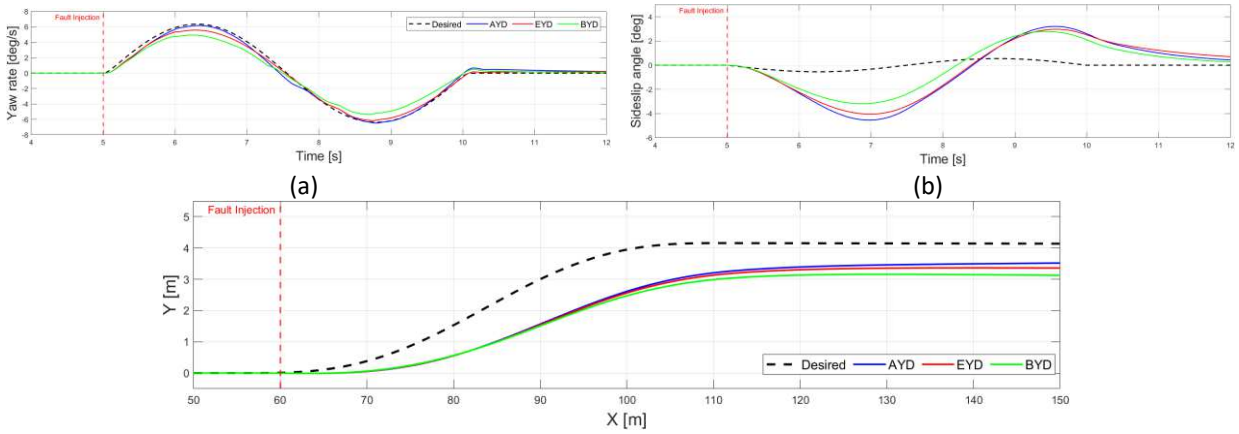
The FTC system performance under complete SbW failure was quantitatively evaluated. The proposed AYD strategy was validated in a simulation environment that ensured both safety and experimental repeatability. A high-fidelity vehicle model based on the nonlinear tire model implemented in IPG CarMaker was employed, and the model fidelity was enhanced by incorporating the same vehicle specifications and actuator degrees of freedom consistent with those of the experimental vehicle system. The simulation and control sampling periods were set to 1 and 10 ms, respectively, to emulate a real-time control environment. To compare the behavioral characteristics under SbW failure with those observed in the actual experimental vehicle, the differences in vehicle dynamic responses corresponding to TV and RWS yaw-moment distribution schemes were analyzed for an OA electric vehicle system. Figures 5(a) and 5(b) show the lane-change simulation results obtained by applying a 20° steering input with a frequency of 0.2 Hz to a vehicle traveling at 40 km/h under complete SbW failure conditions. Consistent with the results of the previous vehicle experiments, the simulation results also showed that the yaw-moment distribution ratio influenced the vehicle dynamic characteristics.

The FTC system performance was quantitatively evaluated by comparing three control strategies. These strategies differed only in the target yaw-moment allocation ratio, whereas all other system components were configured identically. The performance of each control strategy was evaluated using the root mean square error (RMSE) of the tracking errors.



(a) (b)

Fig. 5 Comparison of tracking errors for different yaw-moment distribution ratios under complete SbW failure.



(a) (b)

(c)

Fig. 6 Yaw-rate, sideslip angle, and trajectory responses during a lane-change maneuver.

1. Baseline fixed-ratio yaw-moment distribution (BYD): This strategy allocates the target yaw moment at a fixed ratio of 5:5 between the longitudinal and lateral components.
2. Empirically tuned fixed-ratio yaw-moment distribution (EYD): This strategy applies fixed distribution ratios that were experimentally determined for each driving scenario.
3. AYD: This is the proposed strategy, in which the distribution ratio is adjusted in real time based on the sensitivities of TV and RWS to the vehicle states and SbW actuator dynamics.

The lane-change scenario results shown in Figs. 6–8 were obtained under a steering input of 20° at a frequency of 0.2 Hz while the vehicle traveled at 40 km/h. A complete SbW failure was injected at 5 s, after which the lane-change maneuver was performed with the RWA torque maintained at zero.

The trajectory, yaw-rate tracking error, and sideslip angle tracking error for each yaw-moment distribution strategy in the lane-change scenario are shown in Fig. 6, and the quantitative results are summarized in Table 2. The yaw-rate and trajectory-tracking errors decreases in the order of BYD, EYD, and AYD, as illustrated in Figs. 6(a) and 6(c). In contrast, Fig. 6(b) shows that the sideslip angle errors for the AYD and EYD strategies are larger than that for BYD. This behavior can be attributed to the increased RWS angle resulting from the greater allocation of lateral yaw moment compared with BYD. An increase in the RWS angle enhances the rear lateral tire-force generated by the tire slip angle. This force directly alters the lateral-velocity component of the vehicle and increases the sideslip angle at the vehicle CoG.

Fig. 7 shows the driver steering input, front and rear-steering angles, vehicle speed, and distributed longitudinal and lateral yaw moments for each strategy in the lane-change scenario. The driver steering input and vehicle speed are maintained under identical conditions for all strategies, as shown in Figs. 7(a) and 7(d). As shown in Fig. 7(c), the AYD and EYD strategies generate larger lateral yaw moments than the BYD strategy, resulting in larger RWS angles. This induces front tire slip angle and increases the unintended front-wheel steering due to lateral forces acting at the

FTC Strategy	Position (RMSE)	Yaw rate (RMSE)	Sideslip (RMSE)
AYD	0.998	0.251	1.50
EYD	1.062	0.270	1.41
BYD	1.162	0.574	1.10

Table 2. Tracking performance of different yaw-moment distribution strategies during a lane-change maneuver.

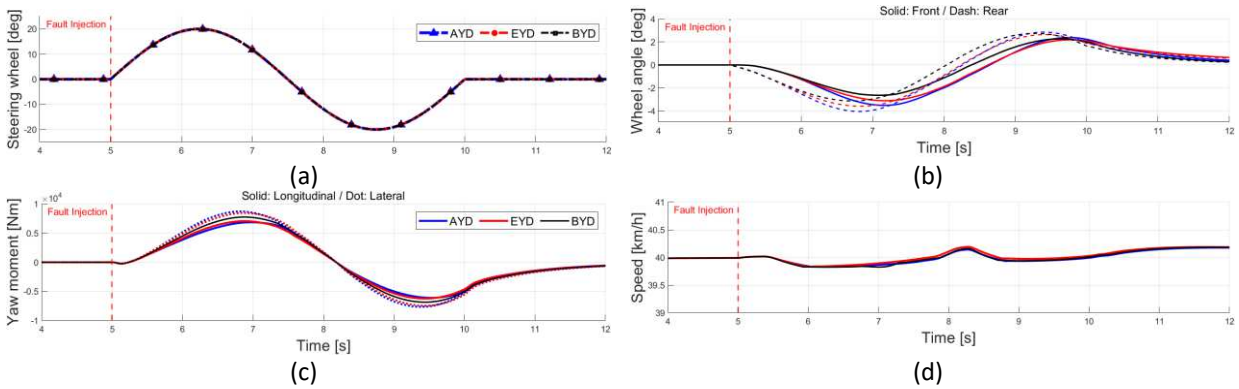


Fig. 7 Steering-wheel angle, wheel-angle, yaw-moment, and speed responses during a lane-change maneuver.

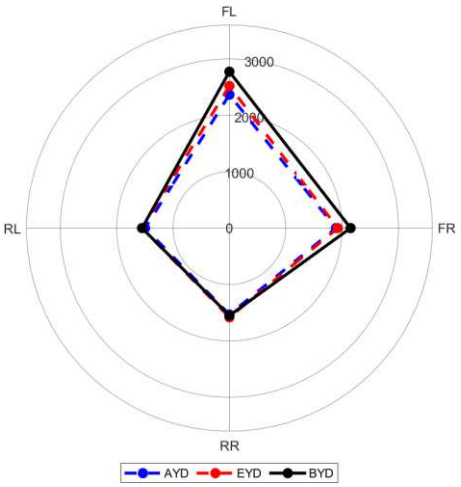


Fig. 8 Combined EMB and e-AWD torque generated by TV during a lane-change maneuver.

end of the pneumatic trail. Consequently, although RWS contributes substantially to the immediate generation of yaw response in transient phases, these results indicate that its use should be regulated by considering both the induced unintended front-wheel steering and the frequency characteristics of the steering input. Fig. 7(b) shows the unintended front-wheel steering induced under complete SbW failure. Fig. 8 shows the summed driving and braking torque outputs of the four wheels for each strategy during the lane-change maneuver. The EYD and AYD strategies, which allocate a smaller portion of the yaw moment to longitudinal components, require lower overall wheel torque demand compared with the BYD strategy, which distributes the yaw moment equally.

The Automated Stopping when Entering the Circle scenario was implemented in accordance with DIN 70065[28], a functional safety standard that defines the degradation evaluation criterion for SbW failure. The corresponding results are presented in Figs. 9–11. This test primarily assesses vehicle controllability after the occurrence of an SbW fault, and lane departure is used as the acceptance criterion. In this scenario, immediately after SbW failure, the vehicle enters a circular path with a radius of 100 m at a speed of 50 km/h and is required to remain within the lane while decelerating at 0.3 g until it comes to a complete stop.

The trajectory, maximum lateral deviation, yaw-rate tracking error, and sideslip angle tracking error for each strategy in the DIN scenario are shown in Fig. 9, and the corresponding quantitative results are summarized in Table 3. Results show that the maximum lateral deviation and yaw-rate tracking errors decrease in the order of BYD, EYD,

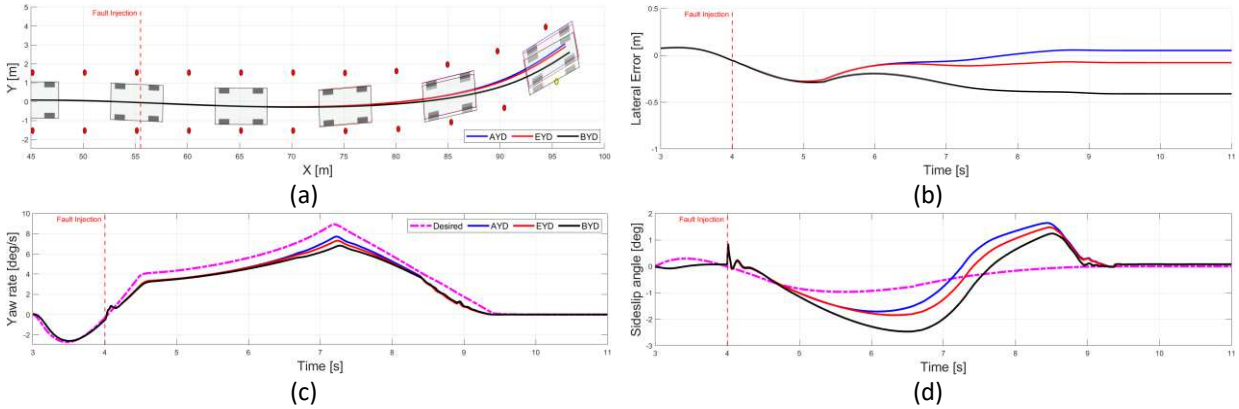


Fig. 9 Trajectory, lateral deviation, yaw-rate, and sideslip angle responses during the DIN circle scenario.

FTC Strategy	Max lateral deviation (m)	Yaw rate (RMSE)	Sideslip (RMSE)
AYD	0.275	0.543	0.521
EYD	0.277	0.601	0.512
BYD	0.410	0.698	0.592

Table 3. Tracking performance of different yaw-moment distribution strategies during the DIN circle scenario.

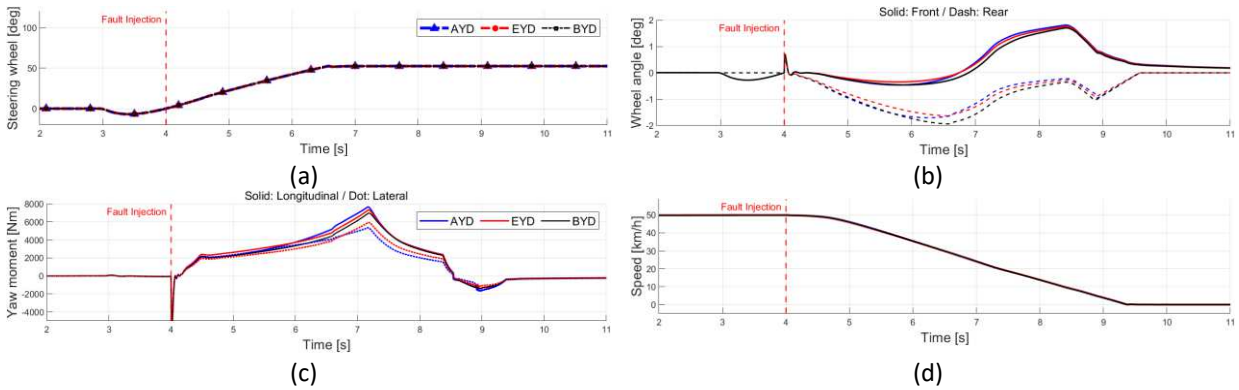


Fig. 10 Steering-wheel angle, wheel-angle, yaw-moment, and speed responses during the DIN circle scenario.

and AYD (Figs. 9(b) and 9(c)). Fig. 9(d) shows that the sideslip angle errors for the AYD and EYD strategies are lower than that for the BYD strategy. Fig. 9(a) shows that the AYD and EYD strategies satisfy the DIN degradation criterion, whereas the BYD strategy makes contact with a pylon during the stopping process and therefore fails to satisfy the criterion.

Fig. 10 shows the driver steering input, front and rear-steering angles, vehicle speed, and distributed longitudinal and lateral yaw moments for each strategy in the DIN scenario. The driver steering input and vehicle deceleration are maintained under identical conditions for all strategies, as shown in Figs. 10(a) and 10(d). As shown in Fig. 10(c), the AYD and EYD strategies allocate a larger longitudinal yaw moment compared with the BYD strategy. Consequently, the longitudinal differential wheel torque generated by TV becomes larger, producing a stronger scrub moment that reduces the unintended front-wheel steering. In particular, after the initial transient phase immediately following entry into the circular path, tracking performance improves during the steady-state phase, as TV induces front-wheel steering in the direction of the turn. Fig. 10(b) shows that the unintended front-wheel steering under complete SbW failure is guided toward the turning direction by TV. Fig. 11 shows the summed driving and braking torque outputs of the four wheels for each strategy in the DIN circle scenario. The EYD and AYD strategies, which allocate a larger portion of the yaw moment to longitudinal components, require higher overall wheel torque demand compared with the BYD strategy, which distributes the yaw moment equally.

Among the three strategies, AYD achieves the lowest yaw-rate tracking error, and lateral deviation distance over the entire maneuver. This strategy increases the lateral yaw moment during the transient phase and gradually increases

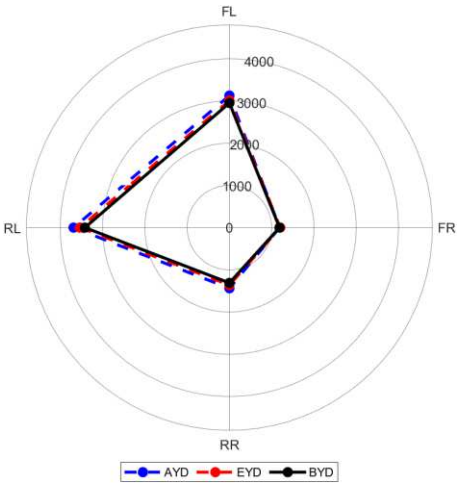


Fig. 11 Combined EMB and e-AWD torque generated by TV during the DIN circle scenario.

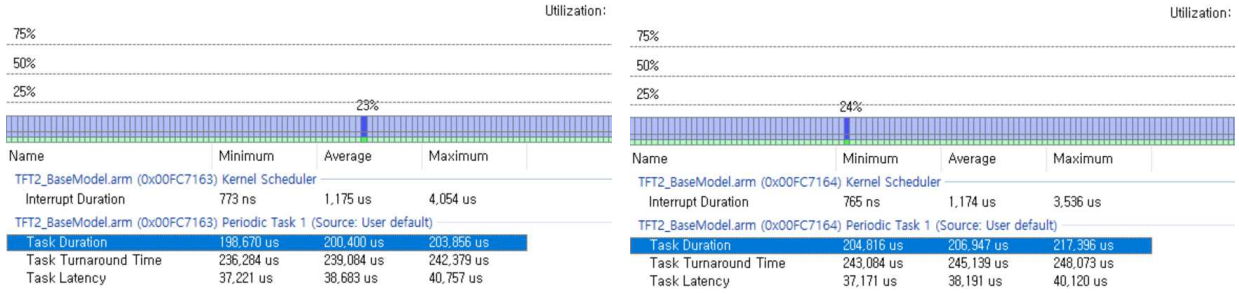


Fig. 12 Real-time task duration results of the proposed FTC system on the RCP platform.

FTC Strategy	Task duration [ms]		
	Minimum	Average	Maximum
AYD	0.204	0.206	0.217
EYD	0.198	0.200	0.203

Table 4. Minimum, average, and maximum task duration of different FTC strategies on the RCP platform.

the longitudinal yaw moment as the vehicle transitions to the steady-state condition. Consequently, the RWS angle increases during the transient steering-response phase to enhance yaw responsiveness, whereas the wheel torques generated by TV increase during the transition to the steady-state phase, thereby inducing front-wheel steering toward the vehicle turning direction. These results indicate that dynamically adjusting coordinated control inputs based on vehicle states under the driving condition and SbW fault characteristics effectively improves fault-tolerant control performance of the OA vehicle platform.

To account for variations in vehicle states and actuator dynamics, the FTC system must ensure real-time computational capability. The computational performance of the proposed strategy was evaluated by comparing it with the conventional EYD-based FTC system implemented on the experimental vehicle, while keeping all system configurations identical except for the yaw-moment distribution strategy. The real-time computational performance of the SbW-FTC system is shown in Fig. 12, and the corresponding quantitative results are summarized in Table 4. Fig. 12(a) shows the computational performance of EYD, and Fig. 12(b) shows that of the proposed AYD strategy. Results indicate that the proposed AYD strategy increases the average computation time by approximately 0.006 ms compared with the EYD strategy. As microprocessor clock speed is a metric of computational capability, the dSPACE MicroAutoBox III, a research-oriented rapid control prototyping (RCP) device, features a 1.4 GHz processor[29], whereas the AURIX TC399, a high-performance automotive microcontroller unit (MCU), operates at 300 MHz[30]. Even when considering a production-vehicle environment with a clock speed approximately four to five times lower

than that of the RCP platform, the proposed AYD-based FTC system remains feasible for real-time implementation in production-vehicle MCU environments.

Conclusion

In this study, an AYD strategy for fault-tolerant steer-by-wire control in OA electric vehicle systems. The proposed method accounts for unintended front-wheel steering under complete SbW failure and incorporated this effect into an integrated vehicle model. Based on this model, the desired yaw moment was dynamically distributed between TV and RWS according to the driving condition. Simulation results revealed that the proposed AYD strategy improved tracking performance under complete SbW failure. The AYD achieved the lowest trajectory and yaw-rate tracking errors in the lane-change scenario and satisfied the DIN 70065 degradation criterion. In addition, the real-time computational performance of the method was suitable for real-time implementation in production-vehicle MCUs. Future work will focus on enhancing the control stability of the FTC system by considering the potential instability caused by driver intervention.

Data availability

The datasets used during the current study are available from the corresponding author on reasonable request.

References

1. Kazemi, R. & Mousavinejad, I. A comprehensive model for developing of steer-by-wire system. Int. J. Mech. Aerosp. Ind. Mechatron. Eng. 5, 2–8 (2011).
2. Mortazavizadeh, S. A., Ghaderi, A., Ebrahimi, M. & Hajian, M. Recent developments in the vehicle steer-by-wire system. IEEE Trans. Transp. Electrification 6, 1226–1235 (2020).
3. Al Sakka, M. et al. Review of fault tolerant multi-motor drive topologies for automotive applications. Energies 15, 5529 (2022).
4. Jung, D. & Kim, S. Hardware-in-the-loop simulation of synchronous motion control for dual-motor driving steer-by-wire system integrated with optimal finite preview path-tracking control. IEEE Trans. Veh. Technol. 73, 3311–3328 (2024).
5. Zong, C., Xiang, H., He, L. & Sha, F. Study on control method of dual-motor for steer-by-wire system. in 2012 2nd International Conference on Consumer Electronics, Communications and Networks (CECNet) 2890–2893 (2012).
6. Yang, J. et al. An adaptive sliding mode fault-tolerant control of variable speed reaching law for steer-by-wire systems. Sci. Rep. 15, 12846 (2025).
7. Haddad, A., Aitouche, A. & Cocquempot, V. Fault tolerant control for autonomous vehicle by generating references for rear wheels steering. IFAC Proc. Vol. 45, 328–333 (2012).
8. Wang, X., Qiu, G. M., Qiang, Z. L. & Hua, Z. J. Research on brake-by-wire system and stability cooperative control for automatic emergency steering. in 2022 IEEE 10th Joint International Information Technology and Artificial Intelligence Conference (ITAIC) 1764–1768 (2022).
9. Hayama, R., Higashi, M., Kawahara, S., Nakano, S. & Kumamoto, H. Fault-tolerant automobile steering based on diversity of steer-by-wire, braking and acceleration. Reliab. Eng. Syst. Saf. 95, 10–17 (2010).
10. Hu, C., Wang, R., Yan, F. & Karimi, H. R. Robust composite nonlinear feedback path-following control for independently actuated autonomous vehicles with differential steering. IEEE Trans. Transp. Electrification 2, 312–321 (2016).
11. Dong, J., Li, J., Gao, Q., Hu, J. & Liu, Z. Optimal coordinated control of active steering and direct yaw moment for distributed-driven electric vehicles. Control Eng. Pract. 134, 105486 (2023).
12. Noh, S. & Kwon, B.-S. Fault tolerant control strategy for four wheel steer-by-wire systems. J. Auto-Veh. Saf. Assoc. 15, 13–20 (2023).
13. Wu, J., Zhao, W., Zhang, B., Wang, C. & Luan, Z. Fault tolerant control of 4WIS based on failure event triggering and self-reconstruction model. IEEE Trans. Transp. Electrification 11, 3502–3513 (2024).
14. Zhang, Y. et al. Fault diagnosis and fault tolerant control for distributed drive electric vehicles through integration of active front steering and direct yaw moment control. Mechatronics 97, 103116 (2024).
15. Ji, Y. et al. Fault-tolerant vehicle stability control based on active steering and direct yaw moment with finite-time constraint performance recovery. IEEE Trans. Veh. Technol. 72, 15317–15329 (2023).
16. Liu, Y. et al. Fault-tolerant control approach based on constraint control allocation for 4WIS/4WID vehicles. Proc. Inst. Mech. Eng. Part D J. Automob. Eng. 235, 2281–2295 (2021).
17. Lu, A., Yu, Y., Li, R. & Tian, G. Advanced fault-tolerant strategies and quantification for 4WID-4WIS vehicles with actuator faults. Proc. Inst. Mech. Eng. Part D J. Automob. Eng. (2025).
18. Jeong, Y. Model predictive control based integrated fault tolerant controller for autonomous vehicles with four-wheel independent steering, driving and braking systems. Veh. Syst. Dyn. 63, 2062–2085 (2025).
19. Ha, Y., Jeon, S., Sorniotti, A. & Woo, S. Comparative study of fault-tolerant control strategies for complete steer-by-wire failures. Control Eng. Pract. 170, 106812 (2026).

20. Huang, C. & Li, L. Architectural design and analysis of a steer-by-wire system in view of functional safety concept. Reliab. Eng. Syst. Saf. 198, 106822 (2020).
21. Emmanuel, L. A., Mbaocha, C. C. & Olubiwe, M. Design of two-degree-of-freedom (2DOF) steering control for automated guided vehicle. Int. J. Sci. Eng. Sci. 3, 57–64 (2019).
22. Dominguez-Garcia, A. D., Kassakian, J. G. & Schindall, J. E. A backup system for automotive steer-by-wire, actuated by selective braking. in 2004 IEEE 35th Annual Power Electronics Specialists Conference 1, 383–388 (2004).
23. Rajamani, R. Vehicle Dynamics and Control 2nd edn (Springer, 2012).
24. Tian, X., Qin, H. & Bao, X. Lateral stability control of brake-by-wire vehicles. in 2021 3rd International Conference on Artificial Intelligence and Advanced Manufacture 2614–2619 (2021).
25. Sun, X., Wang, Y., Cai, Y., Wong, P. K. & Chen, L. An adaptive nonsingular fast terminal sliding mode control for yaw stability control of bus based on STI tire model. Chin. J. Mech. Eng. 34, 79 (2021).
26. Wada, N., Fujii, K. & Saeki, M. Reconfigurable fault-tolerant controller synthesis for a steer-by-wire vehicle using independently driven wheels. Veh. Syst. Dyn. 51, 1438–1465 (2013).
27. Jiang, K., Pavelescu, A. & Charara, A. Estimation of vehicle's vertical and lateral tire forces considering road angle and road irregularity. in 2014 IEEE 17th International Conference on Intelligent Transportation Systems (ITSC) 342–347 (2014).
28. DIN. Road vehicles—Requirements for a Steer-by-Wire (SbW) system (DIN 70065:2024-05, 2024).
29. Stano, P. et al. On-board electric powertrain control for the compensation of the longitudinal acceleration oscillations caused by road irregularities. Mech. Mach. Theory 202, 105759 (2024).
30. Adly, S., Moro, A., Hammad, S. & Maged, S. A. Prevention of controller area network (CAN) attacks on electric autonomous vehicles. Appl. Sci. 13, 9374 (2023).

Author contributions

S.J. formulated the research problem, conducted the simulations, analyzed the results, and wrote the main manuscript text. Y.H. contributed to the research concept and software design, and validated the study. A.S. reviewed the manuscript. S.W. contributed to project administration and provided comments for manuscript revision. All authors read and approved the final manuscript.

Funding

This work was supported by the BK21 Four Program (2120240815267) of the National Research Foundation of Korea (NRF) funded by the Ministry of Education, Korea.

Declarations

Competing interests

The authors declare no competing interests.

Additional information

Correspondence and requests for materials should be addressed to S.J.